Post-Print

This is the accepted version of:

Monito-Ring: an Original FO System for Morphing Application

Monica Ciminello[1], Paolo Bettini[2], Salvatore Ameduri[1], Erika Guerreschi[2], Antonio Concilio[1] and Giuseppe Sala[2]

[1]*C.I.R.A. Italian Aerospace Research Center - Smart Structures Lab, Via Maiorise Capua (CE), Italy*
[2]*Politecnico di Milano – Dipartimento di Scienze e Tecnologie Aerospaziali, Via La Masa 34, 20156 Milano Italy.*

ABSTRACT: An original Monito-Ring system based on chirped fiber optic and DTG array is presented.. The target of this research activity is the realization of a device able to measure deformations of morphing structures which may show large, global displacements due to non-standard architectures and materials adopted. The occurring strain field results, in turns, much more than the standard sensors can handle. Modulations are then necessary to keep the measured strain low. The proposed solution was conceived to overcome this limitation assuring a suitable reduction of the revealed strain. The concept is made of a flexible ring pinned on a certain number of points to the structural component of interest. The fiber optic is integrated within the ring and depending on the angular position of the sensor the ratio between the diameter elongation (i.e. structural strain) and the measured deformation (strain) can be almost arbitrarily set in a large range of values. From each spectrum provided by DTG array, the corresponding unknown strain field is retrieved by applying an inverse technique obtaining an accurate continuous strain map. This article deals with a proof of concept analytical study first, and then numerical and experimental validation.

Key Words: fiber optic, chirped sensor, DTG array, strain sensor, morphing structure

NOMENCLATURE

AAW	*Adaptive Aeroelastic Wing*
ATED	*Adaptive Trailing Edge Device*
CFRP	*Carbon Fiber Reinforced Plastic*
DTG	*Draw Tower Grating*
EC	*European Community*
EU	*European Union*
FBG	*Fiber Bragg Grating*
FEM	*Finite Element Model*
FO	*Fiber Optic*
FP-8	*Framework Program – 8*
GRA	*Green Regional Aircraft*
HECS	*Hyper-Elliptic Cambered Span*
MAW	*Mission Adaptive Wing*
JTI	*Joint Technology Initiatives*
OSA	*Optical Spectrum Analyzer*
POF	*Polymer Optical Fiber*
SC-DTG	*Spectral Continuity Draw Tower Grating*
SD-DTG	*Spectral Discontinuity Draw Tower Grating*
SHM	*Structural Health Monitoring*

INTRODUCTION

In the view of improving aircraft performance, a concept that is more and more gaining space in the future aircraft design perspectives, is structural morphing.

Examples of precursors in developing morphing aircraft include the AFTI/F-111 MAW with its variable camber wing (Cestnik, 2004), the AAW with twist control (Wilson, 2002) and NASA's HECS wing (Davidson, 2003). In all these attempts, the morphing aircraft exhibits tenable aerodynamic properties to suit the needs of multi-mission roles (Figure 1).

Figure 1. Biologically inspired morphing aircraft: sliding skin (Raytheon, sweep angle changes) (Weisshaar, 2003).

A more recent massive cluster devoted to this topic is the SARISTU Project, sponsored by the EU inside the VII Research Framework Programme, (2012) focusing on Smart Intelligent Aircraft Structures. One of the targets is the chord- and span-wise adaptive trailing edge camber variations setting and chasing the best lay-out as a function of the particular and transforming reference state. This has been accomplished by a multifunctional skin (Al-foam composed) and multi-body ribs (Ameduri, 2013; Pecora, 2012).

Another example of attaining morphing structures is to use particular geometries like chiral composite structural networks (Figure 2) that can be manufactured by assembling thin carbon/epoxy or glass/epoxy composite laminates (Bettini, 2009).
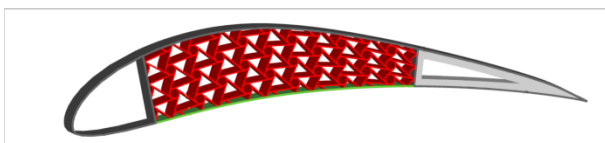

Figure 2. Morphing structures geometries of chiral composite structural network.

All these architectures have in common the objective of realizing wings that can accommodate the variations occurring during a typical mission or between mission and mission, by changing their shape.

When morphing capabilities are taken into consideration, large displacements are in turn usually linked to large strains (magnitude between 1 and 10%.).

This characteristic and the necessity of avoid improbable or impracticable architectures due to classical wired devices on the other, bring to a very hard sensor down-selection. Because the upper limit of commercial and standard monitoring solution based on direct strain measurement is typically set at 1%, modulations are necessary to keep range within the instrumentation capability. Sometimes tailored modulation devices must be addressed for non-standard architecture like the morphing skeleton geometry sketched in Figure 3.
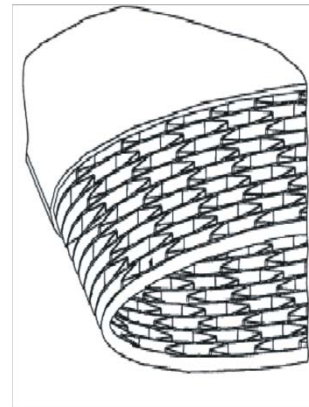

Figure 3. Morphing skeleton concept.

This paper addresses a novel strain-displacement modulator suited for adaptive structures applications. The system is made of a flexible ring with sensors integrated along its path. The proposed device geometry can be easily integrated within morphing skins or grid panels (Totaro, 2012), (Figure 4) to measure strain induced by large displacement.
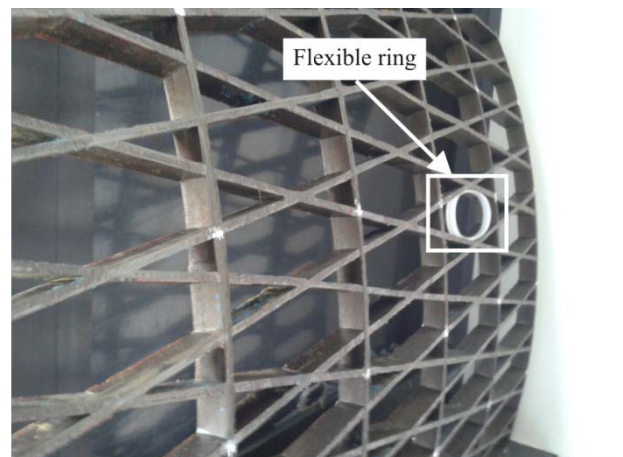
Figure 4. Anisogrid panel extracted from the prototype realized at CIRA for an inter-stage structure.

Two different class of sensors are practicable: wireless, (Karalis, 2008), and fibre optic, (Kiekendall, 2004). The first approach is being currently experienced over a large quantity of ground systems with good success. An example in aeronautical field is described in referenced work (Akl, 2007). The results obtained are used to demonstrate the merits and

potential of this new class of sensors as a viable means for monitoring the deflections of 1D morphing structures. The output of the sensor network is wirelessly transmitted to a control processor to compute the local linear and angular deflections, the global shape and overall strain maps. Complications due to transmission protocols, internal structural configuration requirements, power supply and so on, let however foresee a long path before this kind of systems can actually be flyable.

On the other side, while keeping to some extent contraindication of the classical systems (like cabling, continuous deployment, and so on), fiber optic may lead to a dramatic reduction of the channels number and the wiring needs, above all thanks to an extreme multiplexing capability (see for instance, among the huge literature about, Jones, 1996; Stephan, 2009). Furthermore, the use of the "light" as "information carrier", permits dealing with nimbler, non-shielded wires and avoids any kind of interference with the on-board instrumentation, confining to the laser sources and other similar electronic equipment the unavoidable certification issues.

Because FO are usually made of glass, upper strain limitation deals with the same limits of that material properties. There is some literature references dealing with plastic coating optical fiber sensors for high deformations, not necessarily addressed to morphing aeronautical applications.

An example is the crack detection and vertical deflection monitoring in concrete beams using POF sensors (Kuang, 2003) discloses a helical optical fiber sensor based on macro bending losses. The sensor is embedded in concrete and is used to monitor the deformation due to compression. The material of the helical optical fiber was silicone rubber. The range of the deformation and the sensitivity of the sensor were not disclosed.

In another work (Xiao-Ming, 2012), an optical displacement sensor has been proposed and patented. This devise is a multi-looped POFs geometry. The working principle is based on the power loss particularly sensitive to the mechanical bending.

In other works, modulation devices coupled with fiber optics are proposed. For tunnel structural monitoring an angle transducer based on FBG is described. The transducer consists of a metallic plate, with two FBGs glued, one in each side. The variation of angle is function of the plate bending (Quintela, 2010).

A macro bending principle has also been used for weight measurement (Peter, 2003).In this work a modulation device for FO is realized. When the optical fiber is fully and rigidly bonded on a metallic cantilever beam, it is sufficiently sensitive for the measurement of weight.

In this paper a novel architecture is proposed, made of a particular arrangement of a typical fiberglass over a flexible circular structure, that allows modulating the strain for magnitudes. Definitely, the proposed concept is innovative in its architecture, while integrating components of very well-known behaviour.

When a large displacement is applied on the ring device, the FO deformation is modulated by the body strain field distribution. Modulation ratio between the diameter elongation (i.e. structural strain) and the measured deformation (circumferential strain) can be almost arbitrarily set in a large range of values according to the selected curvilinear abscissa.

The ability of the device to monitor very large deformation is dependent on the material used to manufacture the ring. Two rings, one made of isotropic material (7075-T6 aluminum alloy), the other made of anisotropic material (M49 carbon fiber) have been studied.

In particular, DTG array sensors have been used. From the measured spectrum provided by DTG array, the corresponding unknown strain field can be retrieved by applying an inverse technique developed by the authors (Bettini, 2013). This further investigation highlight the Monito-Ring capability of producing a continuous multi-directional strain map.
Then, the Monito-Ring (the name imposed to the proposed device) rate of sensitivity is defined and used to get some important information on the strain modulation. A finite element model is used to simulate and predict the behaviour of the devices.

In the end, on the basis of the numerical predictions, an experimental campaign is carried out. Static case experiments are addressed to point out the effectiveness of the proposed sensing mechanism into revealing predicted strain. The aeronautic reference case for morphing applications is static. Static morphing is associated to a number of important real applications as the adaptive trailing edge development or the adaptive leading edge development (maneuvers or cruise) (Saggere, 1999; Shili, 2008; Sun, 2012). In these cases furthermore, large strain magnitude is definitely more dramatic than into dynamic cases. Truly, dynamic large strains could be disruptive.

The paper ends with a short survey of envisaged applications.

MONITO-RING SYSTEM DESCRIPTION

The structural device

An elastic ring with a small cross section (negligible thickness with respect to the total length) is herein considered, so that it belongs to the class of slender curved beams (Steigenberger, 2000). When such a structure (arbitrary cross section) is subjected to a transverse loads (along the symmetry axes), it will bend. Depending on the nature and the intensity of the external loads, other effects such as twisting and buckling may occur. As a first step, however, the interest is confined to pure bending effects that hold for a lot of practical cases. The following hypotheses are made on the ring geometry and its material:

- Applied load along one of the symmetry axes.
- Constant cross-section and homogeneous material;
- Inextensibility (symmetry axes plane preserved under deformation);

- Any equilibrium configuration is simply closed curve (this preserving instability).

The Monito-Ring system is sensorized by using FO technology. The angular position of the sensor along the ring curvature governs the ratio between the diameter elongation (structural strain in the diameter) and the measured deformation (ring strain at the arc section), that can be then arbitrarily set in a very large range of values, as demonstrated in the following.

The flexible ring can be dimensioned according to the specific structural application without losing the modelling approach. The system can be manufactured in a cylindrical geometry to be pinned or even bonded on a certain number of points (Figure 5) to the structural component of interest.
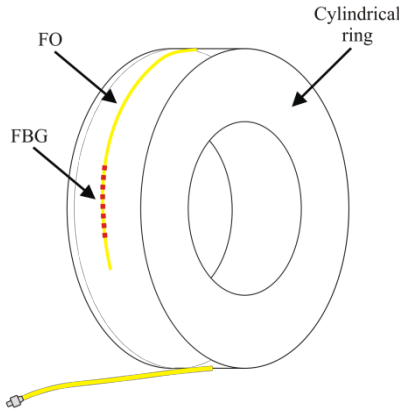

Figure 5. Cylindrical geometry of the Monito-Ring system is sensorized by using FO technology.

This concept belongs to the family of the strain modulators and the main innovation consists in the large modulation capability related to its peculiar geometry. Circular profiles provide, in-fact, several advantages respect to open sections and sharp edges like, for instance, stress concentration lack and the continuity of the monitored field. Moreover a constant curvature allows a simple calibration technique based on a fixed homogeneous strain value in the baseline (no loaded) configuration, which can be evaluated in the design phase, according to the geometrical characteristics. Finally, the deployment of the sensors segments belonging to opposite arches can be used for self-compensated temperature measures, being, this arches subjected to the unsymmetrical tress loads but to the same temperature gradient.

The DTG array and chirped sensor
The Monito-Ring device is integrated by FBG sensors which can ensure a very high sensitivity and high precision, among other advantages. Fiber optic can be bonded or embedded within the ring layers in case composite material is taken into consideration for manufacturing.
The working principle of a standard FBG is based on a periodic change of fiber glass refractive index. In particular, the refractive index change and the grating period remain constant along the fiber axis so that the reflection spectrum exhibits a narrow peak at a specific wavelength λ_B, according to the following Bragg's law:

$$\lambda_B = 2n_{eff}\Lambda \tag{1}$$

The grating period Λ and the effective refractive index n_{eff} are strain dependents as it can be observed in eq. (2) (Hill, 1993). Thus, if a strain ε is applied to the grating, a shift of the reflected Bragg wavelength $d\lambda_B$ can be detected and associated to the average strain of the grating length.

$$\frac{\Delta\lambda_B}{\lambda_{B0}} = \left(\frac{1}{\Lambda_0}\frac{d\Lambda}{d\varepsilon} + \frac{1}{n_0}\frac{dn}{d\varepsilon}\right)\varepsilon + \left(\frac{1}{\Lambda_0}\frac{d\Lambda}{dT} + \frac{1}{n_0}\frac{dn}{dT}\right)\Delta T \tag{2}$$

No information about the strain distribution profile along the grating is generally derived by using this kind of gratings.

Chirped FBGs allow overcoming this limitation. In fact, since both grating period and refractive index linearly increase along the fiber axis, the Bragg wavelength of these sensors is different by the position, resulting in a broad reflection spectrum (see Figure 6). Thus, a spectral-spatial, one-to-one correspondence is gained and a complete strain distribution profile can be retrieved by analyzing the changes of the shape and position of the reflected spectrum.
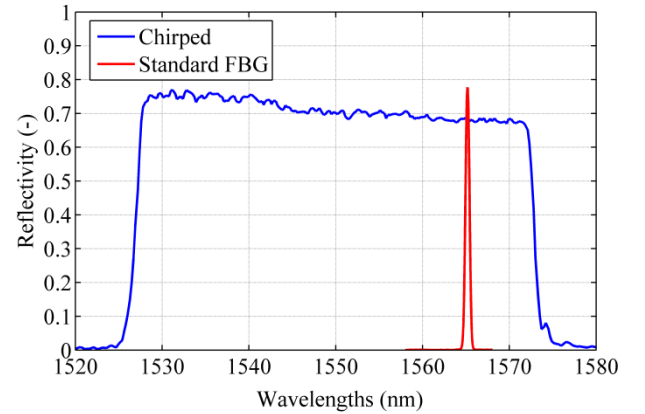

Figure 6. Reflection spectra for uniform and chirped FBG sensors.

In other words the FBG sensors with uniform grating offer local information on the deformation, (i.e. the average strain in a similar manner to a strain gauge), while the chirped one can provide information about the entire monitored profile and therefore seems ideal for structural monitoring. Nevertheless, due to some manufacturing constraints as their limited length and their expensive value on the current market, in order to face with applications as the one proposed in this work, characterized by a distributed and continuous monitoring of the structural element, another optical sensor has also been taken into consideration, known as DTG array.

Due to a recent printing technique, referred to as Draw Tower Gratings (DTG) (DTG Technology, 2012), the grating can be printed before the deposition of the coating, this allowing gratings arrays with very specific spatial and spectral characteristics. In fact, depending to the length, relative

distance of the gratings and its Bragg's wavelengths, different spectral responses can be obtained. For instance, continuum arrays (without gaps between the gratings) can exhibit non continuum spectra as well non continuum arrays can also associated to the continuum spectra.

In this work the following two configurations of DTG arrays are studied:

- spectral discontinuity DTG sensor (SD-DTG): it is an array made by uniform 10mm long gratings spaced of 10mm each so that a continuum spatial configuration can be allowed. The wavelengths correspond to a spectrum composed by well-spaced peaks (red line in figure 7).
- spectral continuity DTG sensor (SC-DTG): it is an array made by uniform 3mm long gratings spaced of 10mm resulting a non-continuum spatial configuration. Due to a smaller length of the individual gratings, the corresponding peaks are more expanded, simulating a spectrum very similar to a chirped one (blue line in Figure 7).
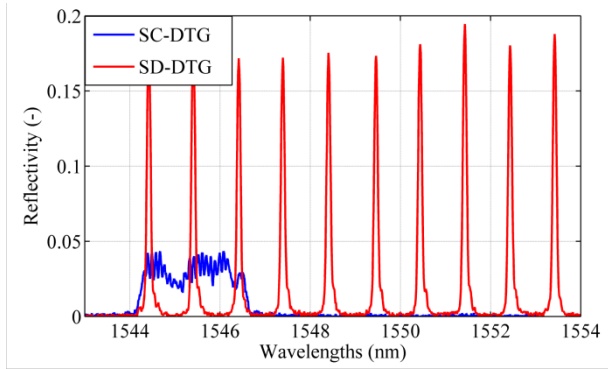
Figure 7. Reflection spectra for different DTG array configurations.

The main characteristics of the adopted DTG arrays are summarized in Table 1, while Table 2 refers to the adopted chirped sensor.

Table 1. Characteristics of the adopted DTG arrays.

Array configuration	SC-DTG	SD-DTG
Total Length (mm)	100	100
Number of FBGs	10	10
FBGs Length (mm)	3	10
FBGs Pitch (mm)	10	10
FWHM (nm)	2.37	-
Chirped rate (nm/mm)	0.0237	-

Table 2. Characteristics of the adopted Chirped FBG.

Sensor type	Chirped
Total Length (mm)	33.5
FWHM (nm)	46.4
Chirped rate (nm/mm)	1.38

ANALYTICAL MODEL

Some methods of handling deformations of elastic rings and curved beams are given in (Ciminello, 2013). Owing to the symmetry of the geometry, only a quarter part can be discussed (Figure 8). It can be parameterized in terms of abscissa and ordinate functions of the curvilinear abscissa:

$$s \rightarrow \big(x(s), y(s)\big) \text{ with } s\epsilon \left[0, \frac{L}{4}\right] \qquad (3)$$

where L is the circumference length, $s=0$ at the clamped-end and $s=L/4$ at the free-end. The load is applied at the free-end.

Let $\theta(s)$ be the curve slope; the following relation holds between the element components, measured in terms of curvilinear abscissa or Cartesian coordinates:

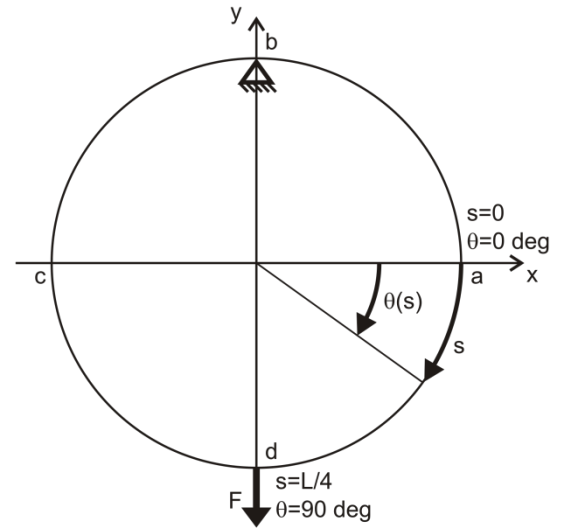$$dx = \cos \theta(s)ds \text{ and } dy = \sin \theta(s)\, ds \qquad (4)$$

Figure 8. Ring geometry: curvilinear abscissa at a circumference quarter.

The bending moment can be related to the cross section inertia I, the Young modulus E and the initial and final curvatures $\theta'(s)$ and $\theta_0'(s)$:

$$M = EI\big(\theta'(s) - \theta'_0(s)\big) \qquad (5)$$

being

$$\theta'(s) = \frac{1}{R} \quad \forall s \qquad (6)$$

following the assumed circular shape of the ring. The difference of first derivative in eq. (5) represents the variation of the ring curvature after and before the deformation is occurred. The moment of inertia I and the modulus of elasticity E of the material are assumed to be invariable. The moment of external force is here defined:

$$F_y \left(y\left(\frac{L}{4}\right) - y_0\left(\frac{L}{4}\right)\right) = \frac{F}{2}\int_0^{L/4}(\sin \theta - \sin \theta_0)ds \qquad (7)$$

being F_y the force acting on the lower point of the ring and $y(L/4)$ and $y_0(L/4)$ the ordinate of this point at the deformed and non-deformed configurations. In the above relation the dependence of the ordinate on the local slope is also considered as:

$$y(s) = \int_0^{s^-} \sin\theta(s)\, ds \qquad (8)$$

Equilibrium occurs when the potential energy is stationary; this is equivalent to solve the following Euler condition:

$$\frac{d}{ds} f_{\theta'} = f_\theta \qquad (9)$$

where:

$$f(s, \theta, \theta') =$$
$$\int_0^{L/4} \left[EI\big(\theta'(s) - \theta'_0(s)\big)^2 - \frac{F}{2}(\sin\theta - \sin\theta_0) \right] ds \qquad (10)$$

Applying (9) to equation (10), the following relations raise up:

$$f_\theta = \frac{F}{2}\cos\theta$$

$$f_{\theta'} = 2EI(\theta' - \theta'_0) \qquad (11)$$

$$\frac{d}{ds} f_{\theta'} = 2EI\theta''$$

Hence the equation (9) can be finally formalized by means of (11) in the following equation (12):

$$\theta'' + \frac{F}{4EI}\cos\theta = 0 \qquad (12)$$

Since the strain on the surface at a distance $t/2$ from the neutral axis, is defined by:

$$\varepsilon(s) = \frac{t}{2}\left(\theta'(s) - \frac{1}{R}\right) \qquad (13)$$

the integration of (12) with the following B.C.:

$$\theta(0) = \frac{\pi}{2}$$
$$\theta\left(\frac{L}{4}\right) = 0 \qquad (14)$$

can be substituted in (13).

On the other hand, if a quasi-static thermodynamic process is assumed, the equation (2) becomes:

$$\frac{\Delta\lambda_B}{\lambda_{B0}} = \left(1 + \frac{1}{n_0}\frac{dn}{d\varepsilon}\right)\varepsilon = (1 - p_e)\varepsilon \qquad (15)$$

and the strain ε can be expressed in function of the shift in Bragg wavelength

$$\varepsilon = \frac{1}{1 - p_e}\frac{d\lambda_B}{\lambda_B} \qquad (16)$$

where p_e is the photo-elastic constant of a generic german-sylicate fiber optic. By comparing (13) and (16), as follows:

$$\frac{t}{2}\left(\theta'(s) - \frac{1}{R}\right) = \frac{1}{1 - p_e}\frac{d\lambda_B}{\lambda_B} \qquad (17)$$

it is possible to define the "curvature" sensitivity coefficient:

$$S = \frac{d\lambda_B}{d\theta(s)} \qquad (18)$$

which, indicates that the sensitivity of the Monito-Ring system can be improved by increasing the value of the radius R or reducing its thickness t.

This theoretical model provides precious information on the behavior of ring made of metallic (isotropic) materials.

In Figure 9, different deformed shapes were plotted, corresponding to different vertical forces applied onto the bottom node. The ring considered for this simulation has a mean radius of 19.8 mm, a thickness of 0.38 mm, a depth of 15 cm and is made of steel (Young modulus of 210 GPa).

In the same graph, also the corresponding shapes obtained by a numerical finite element model were plotted; these results were in good agreement with the theoretical ones.
The strain distribution along a quarter of the arc allows making some interesting consideration. Figure 10 illustrates the strain on the external surface of the ring vs the angular coordinate (90 deg corresponds to the enforced node).
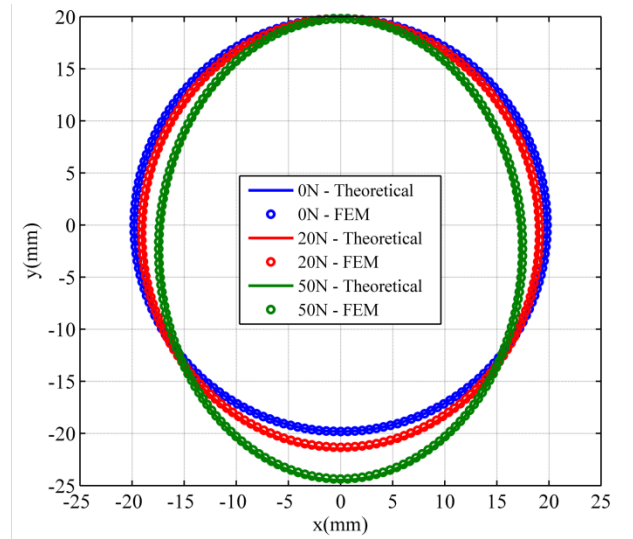

Figure 9. Different deformed shapes corresponding to different vertical forces.

The strain has a maximum on the bottom point (the applied force in fact causes a stretching of the external surface in this zone), while a negative minimum can be found out at the other edge of the quarter (0 deg). Furthermore, as shown in Figure 10(b), a detail of the zero crossing zone, the slope of the curves proved to be strongly dependent on the applied force. Finally also in this picture another important aspect is evident: the zero crossing tends to move rightwards as the load increases, defining in practice a zero crossing domain. This zone, defined on the basis of the expected force range, has to be accurately

avoided during the installation of the FBG sensor, because of the low sensitivity.
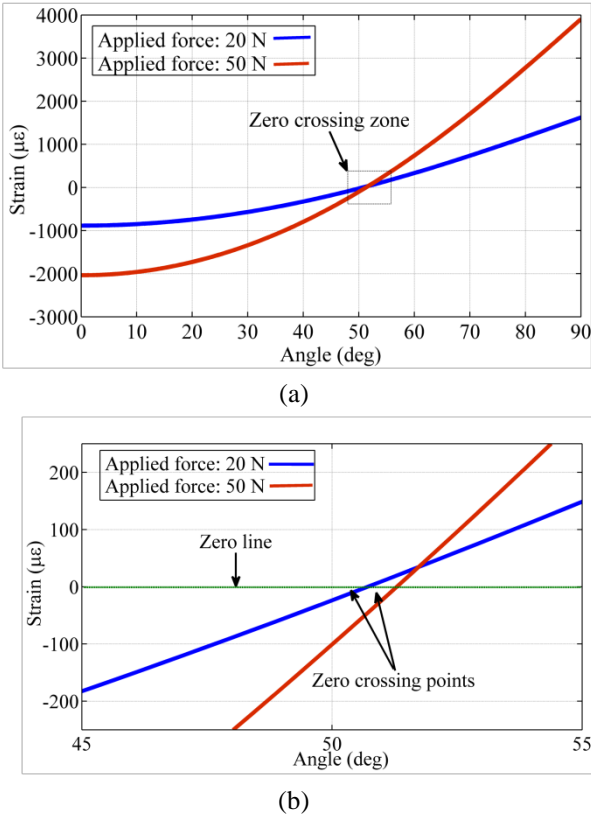

(a)

(b)

Figure 10. Strain on the external surface of the ring vs angular coordinate and zero crossing points: full sector (a), detail of the zero crossing zone (b).

The strain variation along the angular abscissa corresponds to a wide versatility of the ring as strain amplification-reduction device. In fact, on the basis of the specific application (expected displacements), the strain sensor can be bonded close to the edges of the quarter to magnify the deformation, or close to the angle of zero crossing to reduce strain read, thus preventing from eventual damage of the sensor.

NUMERICAL SIMULATION

A finite element approach was adopted to accurately predict and investigate the behavior of rings of different materials: 7075-T6 aluminum alloy and M49 carbon-fiber reinforced plastic (M49-CFRP). The main features and material characteristics are reported in Table 3 and Table 4.

Table 3. Ring geometrical characteristics.

Ring material	Al 7075 T6	M49 CFRP
Ring thickness (mm)	0.68	2.1
Ring width (mm)	15	20
Ring diameter (mm)	40	127.2

The scope of the simulation was essentially to relate the strain of the outside surface of the ring to the displacement of the lower node and the applied force.

Table 4. Ring mechanical characteristics.

Ring material	Al 7075 T6	M49 CFRP
E_{11} (GPa)	70	141
E_{22} (GPa)	70	10
G (GPa)	26.9	6.53
ν	0.3	0.063
Tensile strength limit direction 1 (MPa)	550	2207
Tensile strength limit direction 2 (MPa)	550	81
Compression strength limit direction 1 (MPa)	550	1531
Compression strength limit direction 2 (MPa)	550	81
Shear strength limit (MPa)	331	128

Al 7075 Monito-Ring FEM
The finite element model adopted for the isotropic material (aluminum) is illustrated in Figure 11.
In this case the ring was simulated through 360 BEAM like elements, having the same thickness and depth of the ring.
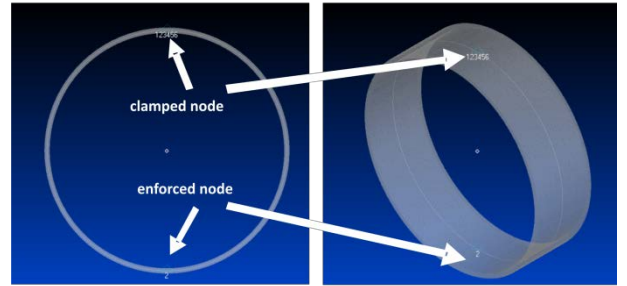

Figure 11. Isotropic ring FE model: frontal view (left), diametric view (right).

The top node was clamped, this way simulating the effect of the upper constraint of the scheme of Figure 11; the displacement of the lower node was enforced.
Static analyses were implemented for increasing vertical displacements. In Figure 12, vertical displacement vs forces is plot.
In Figure 13, deformation vs force is plotted for different arches angle. The theoretical curves were derived by solving eq. (12), for given applied forces F, and then linking (eq. 13) to ϑ coordinate at specific angular positions (0, 30, 45, 60, 90 deg) the corresponding strains.
The large is the angle, the larger is the deviation between numerical and analytic results; this phenomenon can be explained considering that the strong variation of the strain close to 90 deg cannot be punctually estimated by the FEM, due to the finite dimension of the element. This is more evident as the force (and thus the curvature) increases.
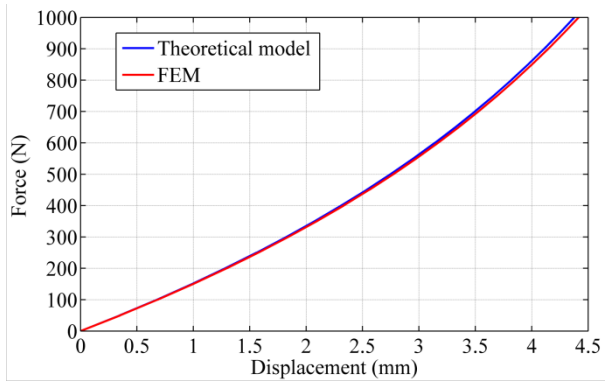
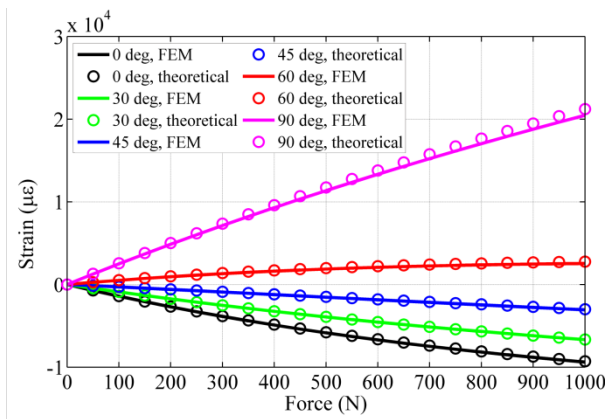**Figure 12.** Vertical displacement vs forces.

Figure 13. Deformation vs force is plot for different arches angle.

Numerical simulation actually confirmed by the mathematical description of the phenomenon.

M49 CFRP Monito-Ring FEM

The choice of the construction of a carbon fiber ring has been made to cope with the need of a ring able to experience high levels of deformation without risking the integrity of the ring itself. To demonstrate the exploitability of a composite ring, two rings of the same size but of different materials (Al 7075-T6 and M49 CFRP, Table 3) were modeled by FE models.

Non-linear static structural FE investigations conducted, showed the possibility of achieving a higher level of vertical elongation (compatible with the structural limitations of the materials of Table 4) using the carbon fiber ring. In practice, with the aluminum ring has reached a maximum displacement of 13.3 mm, while reaching a maximum displacement of 37.0mm using the carbon ring. In Figure 14 the un-deformed and deformed composite ring maximum vertical displacements were compared.

Based on these promising results in terms of increased exploitability, a composite ring was manufactured, whose geometric characteristics are illustrated in Table 3.

Due to the presence of a not negligible thickness variation along the arc length of the manufactured specimen, as reported in Figure 15, an updated FE model matching the specimen

thickness profile was then implemented in order to allow final experimental-numerical correlations.
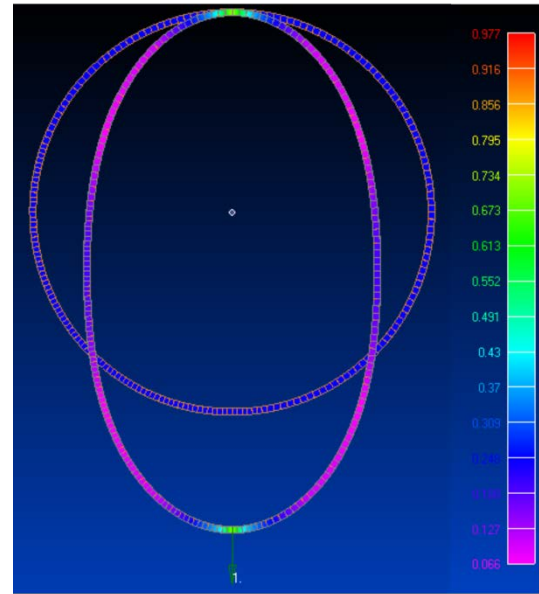

Figure 14. Un-deformed and deformed composite ring maximum vertical displacements.
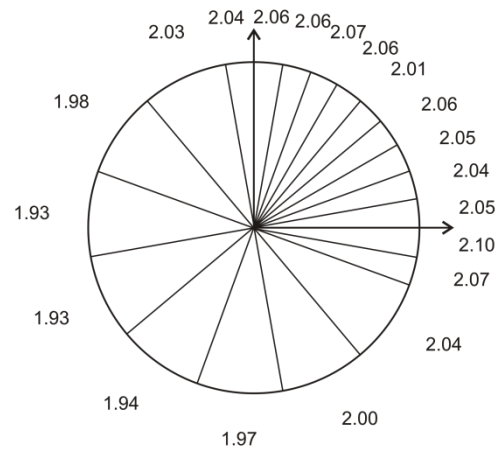

Figure 15. FE model with variable thicknesses map.

The thicknesses are measured in 20 different points along the circumference and are not equally spaced but present more dense mesh in the circumference quarter where the deformations are measured. The ring was modeled by 2D elements, adequately thickening the mesh in the area affected by the measure (i.e. in the area where sensors were bonded).

Force versus displacement and Strain versus angular coordinates curves obtained from FEM simulations are reported in the section "M49 CFRP Monito-Ring test" presented in the next paragraph.

EXPERIMENTAL TEST

The experimental tests were carried out. The following Table 5 summarizes the tested case under considerations.

Table 5. Monito-Ring characteristics.

Ring material	Al 7075 T6	M49 CFRP
Circumference quarter length (mm)	31.4	99.9
FBG length (mm)	33.5	100
FO sensor	Chirped	DTG Array
Strain gauges	4	4

To load the ring along the axial direction, a dedicated steel support has been designed and dimensioned, consisting of two forks which engage the ring by means of two pins as shown in Figures 16-17.

These two forks are connected to an electro-mechanical machine that freezes the bottom bracket and move the top one. The machine measures both force and imposed displacement.

Static test were carried out by applying a load step in time domain. For each load level, measurements from the strain gauges, force and displacement data provided by the Instron machine (Figures 16, 17) and finally the optical sensor spectrum, were acquired.
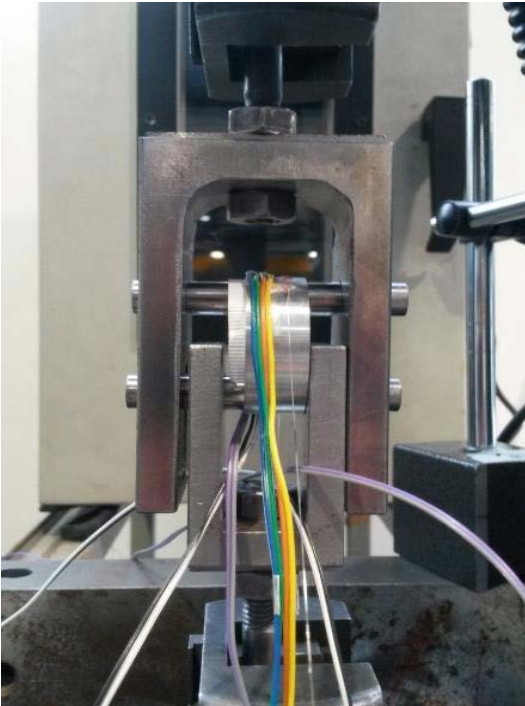

Figure 16. Experimental setup for static test on Al 7075 T6 Ring.

Digital data of the spectra were collected at a simple rate of 1Hz by using an Optical Spectrum Analyzer (OSA) connected with a PC. The light source spectrum was also acquired at the same sample rate in order to be done the data reduction procedure.
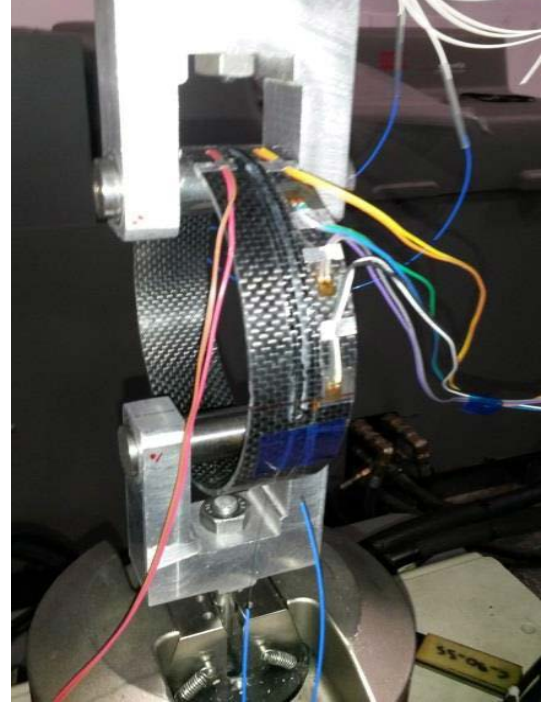

Figure 17. Experimental setup for static test on M49 CFRP ring.

Al 7075 T6 Monito-Ring test

The tests were made starting from the neutral configuration up to an imposed displacement of 2 mm, with intermediate steps of 0.5 mm. A typical fiber optic sensor is able to reach up to 5000 µε, however, to keep a safety margin, it was decided not to exceed the value of 4000 µε and therefore maintain the displacement imposed not above 2 mm. Regarding the mechanical strength of the ring, the 7075-T6 alloy can withstand stresses up to 450 MPa corresponds in this case to about 6400 µε and hence does not represents a limit for the test. The FO was glued with cyanoacrylate in correspondence of a groove made on the surface of the ring having the purpose of allowing the routing of the fiber along the circumferential direction path.

The deformation of the ring was also monitored by a strain gauge chain made of 4 Strain Gauges. Table 6 summarizes the main characteristics of all the adopted strain transducers.

Table 6. Strain sensors position along the ring.

Sensors	Gauge length (mm)	Position (mm)
SG 1	3	2.8
SG 2	3	11.4
SG 3	3	20.2
SG 4	3	28.8
Chirped	33.5	From -2 to 31

The table above also contains the geometrical position of the gauges along the quarter-circle. The origin is considered the point at which the force is applied.

The chirped sensor was longer than the circumference quarter, so, as expected from the analytical description of the system, a zero-crossing strain detection is measured, this means the corresponding spectrum must experience a compression load on one edge and a traction on the opposite one.

In Figure 18 different effects on the spectrum are plotted. Two tests were performed: at first, the ring was mounted having the sensor in the circumference quarter identified by the arc *ad* (see Figure 8: the sensor edge corresponding to the lower spectrum wavelength is positioned in the point *a*); then, the ring was rotated by 90 deg counter clockwise in order to measure the arc *ba* referred at the same figure.

The red spectrum shows the edges moving away if compared with the blue ones (unloaded configuration). This means that the Bragg wavelength decreases on the left due to a compression load and increases on the right due to a traction load. According to the equation 16, the shift of the spectrum left and right edges corresponds to a deformation of about -2000 µε and +4000 µε, respectively.

As expected, the green spectrum (Figure 18), referred to the rotated ring, experiences the inversion of the strain field (the edge on the left increases due to traction and on the right decreases due to compression) and the edges approach. It can be observed from the same figure that, the distance between red and blue edges on the left (corresponding to the traction in rotated configuration) is the same distance between green and blue line on the right (corresponding to the traction in un-rotated configuration). The same consideration can be done for the other couple of edges.
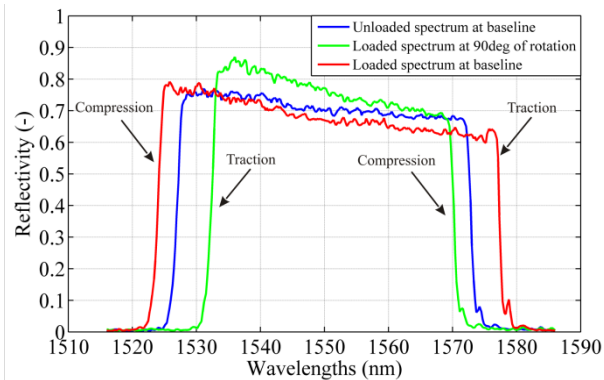

Figure 18. Acquired chirped spectrum referred to different positions of the grating along the ring: spectrum experienced a compression load on the baseline edge of the sensor and a traction load on the opposite one.

Figure 19 compares the analytical strain profile with the experimental results in correspondence of a vertical displacement of 2 mm.
In order to reconstruct the deformed grating strain profile from its reflection spectrum, an inverse procedure has been adopted. After applying a numerical model (based on Couple Mode Theory) able to simulate the spectral response of a grating subjected to a generic strain profile (direct problem), a genetic algorithm and an optimization procedure have been implemented in order to find the strain profile minimizing the difference between simulated and experimental spectra (inverse problem) (Rostami, 2007).
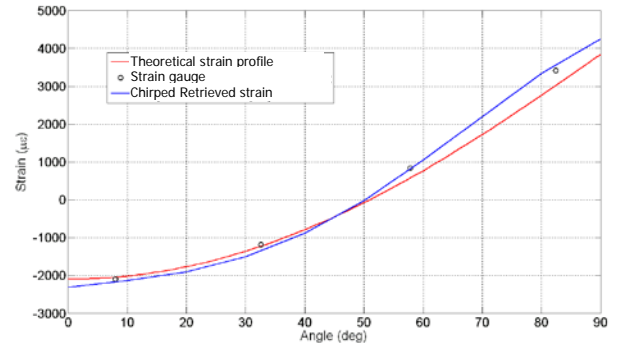

Figure 19. Strain value at different diameter deployment: Al 7075 T6 ring.

The experimental curves are in good agreement with the analytical simulation. Compared to strain gauges, the retrieved solution from chirped acquisitions appears well reliable and a good quality trend was identified.
The maximum error was mainly due to the instability of the available light source. In fact, since the inverse procedure is based on the reflection spectrum normalized respect to the input signals, the results are quite sensitive to the optical intensity variation of the source.

Definitely, starting from the measured strain profiles, the analytical procedure is applied (by using Eq.8) for the diameter elongation estimation (reported in Table 7).

Table 7. Retrieved analytical elongation for Al 7075 T6 ring and comparison with the experimental one.

Applied displacement (mm)	Retrieved displacement (mm)	Error (%)
0.50	0.40	20.4
1.25	1.54	23.2
2.00	2.29	14.5

The percentage errors between the applied displacement and the retrieved one were mainly influenced by the instability of the light source.

M49 CFRP Monito-Ring test
The ring was made of 9 plies of unidirectional carbon fiber M49 epoxy resin, each one 0.24 mm thick (pre-curing thickness). Plies were cut 80 mm wide and of variable length from 387 mm to 400 mm corresponding to the first and the last ply. Each ply was wrapped around the mandrel so as to align the end edges, thus without overlap to avoid abrupt changes of thickness, in this way remains a point of discontinuity for each lamina (Figure 20). These points were equally spaced distributed along the circumference, simply dividing the 360 degrees in 9 equal parts, which is a discontinuity point every 40 degrees.
Finally, the laminate was cured in autoclave at 140 °C and 3 bar of pressure for 60 minutes.

The quasi-static test was carried out by controlling the diameter elongation with a pitch of 2mm, up to a maximum of 8mm which corresponds to an elongation of 6.3% on the diameter and causes a maximum deflection on the circumference quarter of about 4000με, assumed as the limit value in order to avoid FO breaking.

Figure 20. M49 CFRP prepreg laminates made of 9 plies wrapped around the mandrel.

In Figure 21 the experimental force versus displacement curve obtained in a preliminary test is correlated with the FEM analysis in order to verify the matching between the numerical model and the manufactured ring in presence of variable thicknesses as introduced in the previous paragraph.
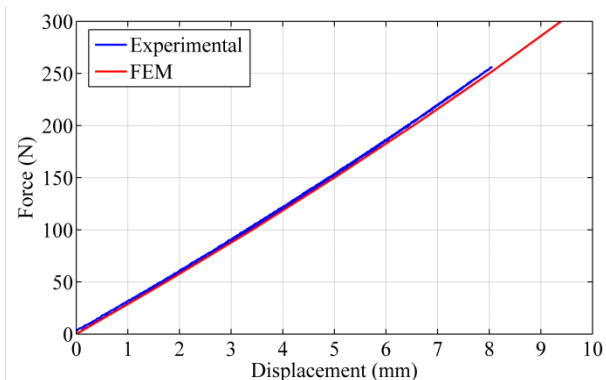

Figure 21. Numerical-Experimental correlation of the Force vs displacement curve.

After that, two DTG arrays with continuous/discontinuous spectral features were installed on the circumference quarter.
The fibers were glued with cyanoacrylate into a surface recess, opportunely manufactured so as to perfectly align the sensors in the circumferential direction.

Four strain gauges were also installed in order to make a comparison of the optical measures.
The table 8 shows the strain gauges geometrical positions along the circumference quarter. The origin is the point at which the force is applied.
Tests were performed using both the two DTG arrays. The spectral continuity array is compared in with numerical and strain gauge data in Figure 22a, while the spectral discontinuity array data were plotted in Figure 22b.

Table 8. Strain sensors position along the ring.

Sensors	Gauge length (mm)	Position (mm)
SG 1	3	1.2
SG 2	3	33.3
SG 3	3	66.6
SG 4	3	98.8
SC-DTG	100	0 to 100
SD-DTG	100	0 to 100
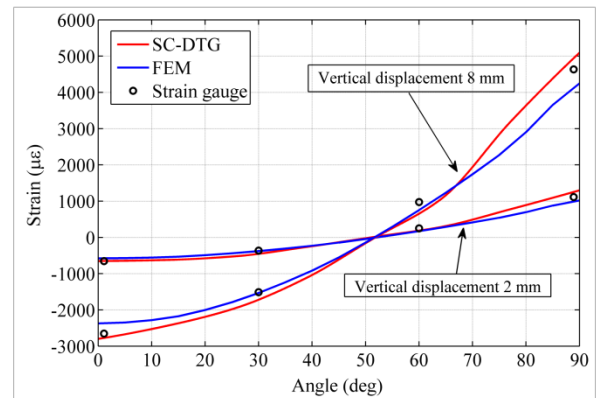
(a)
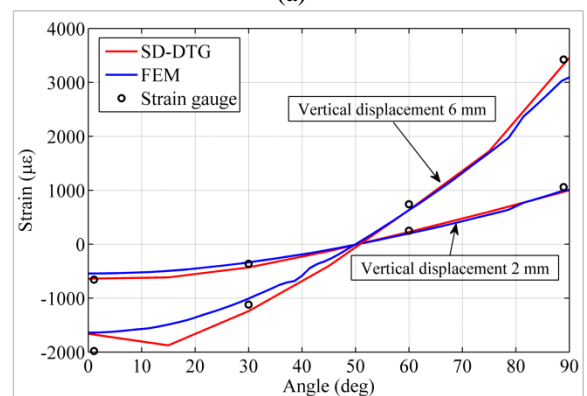
(b)

Figure 22. Strain value at different diameter elongation: a) SC-DTG array; b) SD-DTG array.

In both cases a good correlation was obtained evidencing how the composite material is also adequate to manufacture the Monito-Ring device.

Moreover, the retrieved deformations, which are very close with strain gauges values, confirm that DTG arrays can be adopted in place of chirped FBGs for the inverse procedure. As consequence, a lot of advantages in terms of economical and computational costs may be achieved.
In fact, by properly setting their configuration, DTG arrays becomes equivalent to a continuous chirped sensor and the sum of the narrow spectra of each FBG can be treated as a unique broad spectrum, similar to the chirped one providing an accurate continuous multi-directional strain map. In this way a bigger and cheaper chirped sensor can be obtained (Bettini, 2013).

In the end, from the measured strain profiles, the analytical procedure is applied (Eq. 8) for the calculation of the diameter elongation. Results are shown in table 9.

Table 9. Retrieved analytical elongation for M49 CFRP ring and comparison with the experimental one.

Applied displacement (mm)	Retrieved displacement (mm)	Error (%)
2.00	1.89	5.6
4.00	3.57	10.6
6.00	5.47	8.8
8.00	7.23	9.6

The estimated errors show the goodness of the procedure here applied to retrieve the displacement. Nevertheless, light source instability introduces again some indeterminacy.

FUTURE APPLICATIONS

Dedicated studies to exploit specific morphing applications are planned in the next future steps. Following, a couple of example of envisaged developments is shortly introduced.

It is known that three independent strain measurements (in different directions) are required to determine the unknown principal strains and stresses in a general two-axis stress state. Rosette devices are designed to perform such a function in experimental analysis.

FBG rosettes and electrical strain gauges follow the same work principle; however, optical systems have clear advantages from the installation point of view, for their acknowledged multiplexing capability.

As demonstrated in the previous paragraphs, using DTG array sensors, it is possible to map the region of interest without loss of continuity.

For its adaptive geometry, the Monito-Ring can be an alternative to rosettes, and can also provide added information as shape variation in high curvature regions (see leading edge droop nose, Figure 23), or in morphing grid panels under a large displacement field (Figure 24). Both the suggested applications highlight the strong potentialities of the proposed system in terms of compactness and minimal intrusiveness.
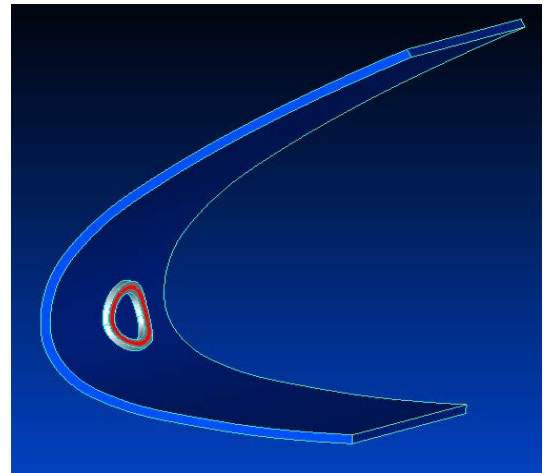

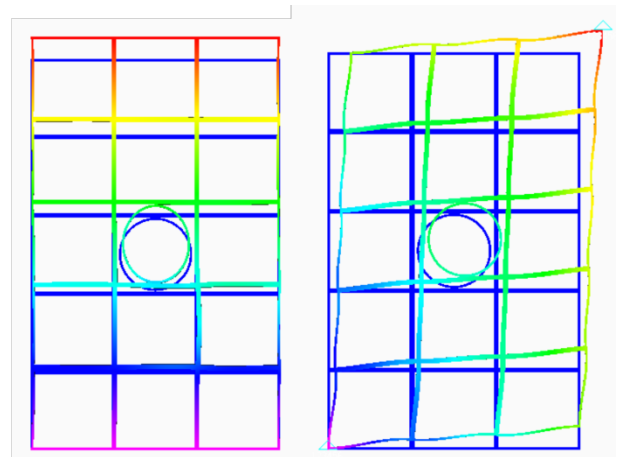**Figure 23.** Leading edge instrumented profile.

Figure 24. Monito-Ring device installed in a grid panel structure - Left: load applied on principal direction; Right: load applied on a generic direction.

CONCLUSIONS

Future morphing structures may show large, global displacements, non-standard architecture and their shapes and health integrity have to be controlled. In addition, when aeronautical applications are considered, the necessity to avoid improbable or impracticable architectures due to classical wired devices is another important issue. FO sensors can satisfy the requirements related to the reduction of cable routing complexity and can be used for large deformation field if embedded in special supporting structure opportunely designed.

A novel ring geometry sensorized with FO is here proposed as strain modulators. Numerical and experimental investigations of Monito-Ring systems made of different materials have been presented.

Experiments are performed to show the basic characteristics and the effectiveness of the proposed strain-displacement sensing mechanism in static conditions as reference for

morphing applications. FBG measures have been successfully compared with strain gauges data.

Preliminary results have shown the ability of carbon fiber ring to reach 8mm of elongation along its diameter, with a corresponding diameter deformation of 60000με. The measured deformation (strain along the circumference) have been measured and verified to be 4000με. Gauge factor can be improved by selecting curvilinear abscissa and manufacturing a Monito-Ring device with smaller Young modulus.

Chirped and DTG array sensor have been integrated on the ring. From each spectrum provided by DTG array, the corresponding unknown strain field can be retrieved by applying a novel inverse technique obtaining an accurate multi-directional strain map very promising for morphing applications.

A study dedicated to the proposed device tied into a specific application and the relatives installation requirements will be treated in detail in further works.

REFERENCES

Akl W, Poh S and Baz A (2007) Wireless and distributed sensing of the shape of morphing structures. *Sensors and Actuators*, 140: 94–102.

Ameduri S, Concilio A and Pecora R (2013) A single slotted morphing flap based on sma technology. In: *6th ECCOMAS Conference on Smart Structures and Materials*, Politecnico di Torino, Italy, 24-26 June 2013. SMART2013.

Bettini P, Airoldi A, Sala G et al. (2009) Composite chiral structures for morphing airfoils: Numerical analyses and development of a manufacturing process. *Journal of Composites: Part B.* DOI:10.1016.

Bettini P, Sala D and Sala G (2013) Numerical and experimental study of fibre Bragg grating sensors for structural health and usage monitoring systems. In: *Italian Association of Aeronautics and Astronautics XXII Conference*, Naples, Italy, 9-12 September 2013.

Cesnik CES, Last HR and Martin CA (2004) A Framework for morphing capability assessment. In: *Proceedings of the 45th AIAA/ASME/ASCE/AHS/ASC on Structures, Structural Dynamics & Materials Conference*, Palm Springs, CA, 19–22 April 2004. Paper AIAA 2004-1654.

Ciminello M, Ameduri S and Flauto D (2013) Design of FBG based-on sensor device for large displacement deformation. In: *Proceedings of IEEE 113971*, Rio de Janeiro, Brasil, 4-7 August 2013. Paper IMOC2013.

Davidson JB, Chwalowski P and Lazos BS (2003) Flight dynamic simulation assessment of a morphable hyper-elliptic cambered span winged configuration. In: *Proceedings of the AIAA on Atmospheric Flight Mechanics Conference and Exhibit*, Austin, TX, 11–14 August 2003. Paper AIAA 2003-5301.

DTG Technology (2012). Available at: www.fbgs.com/technology/dtg-technology

Hill KO and Meltz G (1993) Fiber Bragg grating technology fundamentals and overview. *J. Lightwave Technol.* 15, 78-88.

Jones ME, Duncan PG, Crotts R et al. (1996) Multiplexing optical fiber-based pressure sensors for smart wings. In: *SPIE Proceedings,* 30 May 1996, Vol. 2718.

Karalis et al (2008) Efficient wireless non radiative mid range enrgy transfer. *Annals of Physics*, 323: 34–48.

Kirkendall CK and Anthony DA (2004) Overview of high performance fibre-optic sensing. *Journal of Physics*, 37(18): 197–216.

Kuang KSC et al. (2003) Crack detection and vertical deflection monitoring in concrete beams using plastic optical fibre sensors, Measurement Science and Technology, 14(2) doi:10.1088/0957-0233/14/2/308.

Pecora R, Amoroso F and Lecce L (2012) Effectiveness of Wing Twist Morphing in Roll Control. *Journal of Aircraft*, 49(6): 1666-1674.

Peter CC, Shiping C (2003) Fiber optic strain sensor. *US 6668105 B2*, 23 December 2003.

Quintela A, Lázaro JM, Quintela MA et al. (2010) Angle transducer based on fiber Bragg gratings able for tunnel auscultation. In: *SPIE Proceedings,* 9 September 2010, Vol. 7653: (4 pp).

Rostami A and Yazdanpanah-Goharrizi A (2007) A New Method for Classification and Identification of Complex Fiber Bragg Gratings Using the Genetic Algorithm. *Progress in Electromagnetics Research* 75.

Saggere L, Kota S (1999) Static shape control of smart structures using compliant mechanisms. *AIAA Journal* 37 (5): 572–578

Saristu Project (2012). Available at: www.saristu.eu/project/activities/as-02-structural-tailoring-of-wing-trailing-edge-device (accessed 1 October 2010).

Shili L, Wenjie G, Shujun L (2008) Optimal Design of Compliant Trailing Edge for Shape Changing. *Chinese Journal of Aeronautics*, 21(2):187–192

Steigenberger J, Zimmermann K and Schulte U (2000) On large deformations of elastic rings via phase-plane discussion. *Archive of Applied Mechanics*, 70: 489-507.

Stephan R, Lae-Hyong K, Jae-Hung H et al. (2009) Displacement field estimation for a two-dimensional structure using fiber Bragg grating sensors. *Journal of Smart Material and Structures*, 18: (12pp).

Sun Z, Guo S, Fu Q (2012) Design and Analysis of a Wing Structure with Static Aeroelastic Effect for Optimal Performance. In: *Proceeding of ICCE-20*, Beijing, China, 21-27 July 2012.

Totaro G and De Nicola F (2012) Recent advance on design and manufacturing of composite anisogrid structures for space launchers. *Acta Astronautica,* 81:570-577.

Weisshaar T (2003) The next 100 years of flight—part two. *NewScientist.com.*, News Service.

Wilson JR (2002) Active aeroelastic wing: a new/old twist on flight. *Aerospace America Journal*: 40 (9): 34–37.

Xiao-Ming T et al. (2012) Fiber strain sensor and measurement system for repeated large deformation. *US008276462B2*, 2 October 2012.